

Manifold learning of Poincaré sections reveals the topology of high-dimensional chaotic flows

Evangelos Siminos^{a)}

Department of Physics, University of Gothenburg, SE-41296 Göteborg, Sweden

(Dated: 21 May 2021)

It is shown that applying manifold learning techniques to Poincaré sections of high-dimensional, chaotic dynamical systems can uncover their low-dimensional topological organization. Manifold learning provides a low-dimensional embedding and intrinsic coordinates for the parametrization of data on the Poincaré section, facilitating the construction of return maps with well defined symbolic dynamics. The method is illustrated by numerical examples for the Rössler attractor and the Kuramoto-Sivashinsky equation. For the latter we present the reduction of the high-dimensional, continuous-time flow to dynamics on one- and two two-dimensional Poincaré sections. We show that in the two-dimensional embedding case the attractor is organized by one-dimensional unstable manifolds of short periodic orbits. In that case, the dynamics can be approximated by a map on a tree which can in turn be reduced to a trimodal map of the unit interval. In order to test the limits of the one-dimensional map approximation we apply classical kneading theory in order to systematically detect all periodic orbits of the system up to any given topological length.

When confronted with chaotic dynamical systems, there are different levels at which we may declare our that our aim to understand them has been fulfilled. A classical approach that goes back to the early days of the field is to reduce the continuous time dynamics to a discrete time map on a Poincaré section, a hyperplane that intersects trajectories transversally. That approach, when successful, elucidates the topological organization of the flow and allows one to label different solutions with symbolic sequences and to reduce chaotic dynamics to a “walk” in the space of such sequences known as *symbolic dynamics*. This enhances our understanding of how chaotic dynamics are generated for a given flow and allows dynamical systems to be classified in equivalence classes. Moreover, it allows us to systematically generate and classify the compact solutions that organize chaotic dynamics. However, carrying out such a topological program is far from trivial for high-dimensional dynamical systems, such as fluid flows, even when such systems are known to possess low dimensional attractors. The difficulty lies in the lack of a systematic way to find low dimensional coordinates on the attractor that would lead to useful return maps. Here, it is shown that manifold learning techniques, when applied directly on the Poincaré section rather than on the continuous time flow, can provide a straightforward way to construct low-dimensional return maps.

the Poincaré section technique have allowed to represent low-dimensional dynamical systems as one- or two-dimensional maps and to apply the well developed methods of topological analysis of discrete maps in order to shed insight in the dynamics of the original dynamical system^{1,2}. In particular, this approach allows the spectrum of admissible compact solutions, such as periodic orbits, to be determined and attractors to be classified in topological conjugacy classes. However, this program becomes rather hard to carry out in high-dimensional dynamical systems, for which there is usually no obvious way to choose and parametrize a Poincaré section that would lead to a useful return map. This hinders progress in the study of turbulent fluid flows as high-dimensional dynamical systems for which there has been considerable interest over the last twenty years, see for example Ref.^{3–8}. While the state space of fluid flows, described by partial differential equations (PDEs), is formally infinite dimensional, Lyapunov analysis arguments^{9,10} and the theory of inertial manifolds^{11–13} suggest that the asymptotic dynamics of dissipative PDEs may take place in a finite-dimensional state-space. However, it remains unclear how to construct lower-dimensional representations of fluid flows that could be utilized in dynamical systems studies.

The topic of dimensionality reduction has been pursued in the field of nonlinear dynamics of dissipative PDEs using many different approaches. Linear methods, most notably proper orthogonal decomposition¹⁴ fail to capture the nonlinear structure of the attractor or inertial manifold and are often sub-optimal in terms of number of variables required to faithfully capture the dynamics¹⁵. Nonlinear dimensionality reduction, also known as manifold learning^{16,17} (reviewed briefly in Sec. II B), could be a better alternative since it provides methods to re-embed geometric objects from a high-dimensional to a lower dimensional space, while preserving geometrical or topological structure. While several works, e.g. ^{18–20}, have applied manifold learning techniques to data generated by chaotic dynamical systems, it is still unclear that such methods could help elucidate the topology of high-dimensional dynamical systems, for two reasons. First, such methods need to operate on finely sampled, high-dimensional

I. INTRODUCTION

One of the most successful methods to uncover the topological organization of chaotic attractors is to convert the continuous time flow defined in a state-space of dimension d to a discrete time return map defined on a $d - 1$ -dimensional hypersurface known as a Poincaré surface of section. Variations of

^{a)}Electronic mail: evangelos.siminos@gmail.com

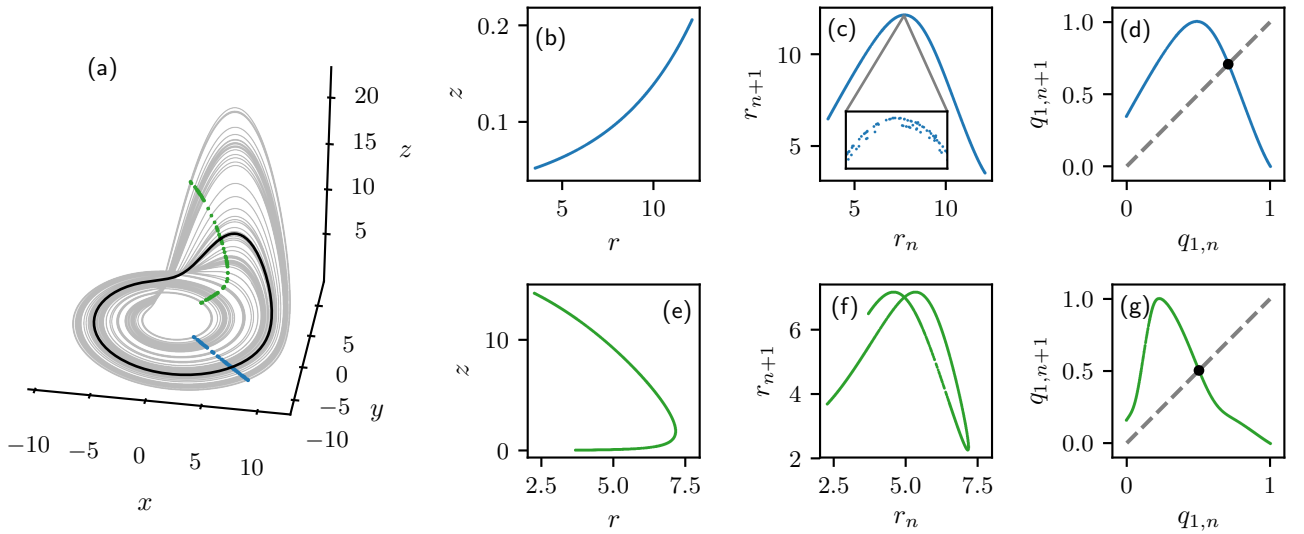


FIG. 1. (a) Long trajectory on the attractor of the Rössler flow (grey), periodic orbit $\bar{1}$ (black), points of intersection with the Poincaré surface of section \mathcal{P}_1 (blue) and \mathcal{P}_2 (green), (b,e) points of intersection with \mathcal{P}_1 (blue) and \mathcal{P}_2 (green) in (r, z) representation, (c,f) corresponding first return maps in the radial variable; the inset in (c) shows an area with dimensions $(\delta r_n, \delta r_{n+1}) = (2.5 \times 10^{-3}, 1.7 \times 10^{-6})$, (d,g) return maps in intrinsic coordinate q found through application of LLE with parameters $K = 160$, $Np = 4372$ and $\epsilon = 1e-3$, along with the diagonal $q_{n+1} = s_n$ (dashed grey line) and the periodic orbit $\bar{1}$ (black dot).

data in order to correctly reproduce the low-dimensional structure, limiting their scalability towards systems with a high-dimensional state-space. Second, even when a low dimensional embedding of, e.g., a chaotic attractor can be obtained, the underlying topology often remains obscure¹⁸.

In this work it is proposed that, for the purpose of reducing a continuous time, high-dimensional dynamical system to low-dimensional return map, nonlinear dimensionality reduction methods should be applied directly on the Poincaré section rather than on the continuous time system. While the introduction of a Poincaré section is associated with a small reduction in dimensionality (from d to $d - 1$ dimensions), it leads to a dramatic reduction in the amount of data required to describe the system, since it eliminates the need to sample trajectories (in time) between successive intersections. As shown in the example of the low-dimensional Rössler flow, Sec. II, manifold learning solves the problem of choosing a suitable surface of section in a natural way, by providing an intrinsic parametrization of (data on) the section. This leads to well defined return maps independently of the choice of surface of section. The method can be seen as a generalization of the idea of using the geodesic distance along ordered periodic points²¹ or one-dimensional unstable manifolds of periodic orbits to parametrize the return map^{22,23}. However, manifold learning is much less restrictive, since it does not require the computation of periodic orbits and their unstable manifolds and can also parameterize multi-dimensional manifolds. This allows us to treat more complicated topologies than hitherto possible.

In order to put this idea to the test for higher-dimensional dynamical systems, the Kuramoto-Sivashinsky partial differential equation (KSe) is studied for two parameter values corresponding to Poincaré section data that can be parametrized

as one- or two-dimensional manifolds in Sec. III B and Sec. III C, respectively. Surprisingly, we find that even in the case of a two-dimensional embedding, a description based on one-dimensional tree maps is possible. Since such tree maps can be somewhat cumbersome to work with, we show that they can be reduced to ordinary maps of the unit interval. In order to illustrate the utility but also the limits of the one-dimensional map approximation and the corresponding symbolic dynamics we use classical kneading theory to systematically determine KSe periodic orbits in Sec. III D. In Sec. III E we examine the organization of the attractor in terms of the one-dimensional unstable manifolds of the shortest periodic orbits and argue that the presented method could be useful whenever dynamics is organized by low-dimensional unstable manifolds.

II. MANIFOLD LEARNING OF POINCARÉ SECTIONS

A. Motivation: Return maps of chaotic flows

To illustrate the problem of Poincaré section choice, and present it in the context of the Rössler flow²⁴, along the lines of Ref.². The Rössler flow reads

$$\dot{x} = -y - z, \quad (1)$$

$$\dot{y} = x + ay \quad (2)$$

$$\dot{z} = b + z(x - c). \quad (3)$$

In the following we choose parameters $a = b = 0.2$, $c = 5.7$, for which Eq. (1) has a chaotic attractor with Kaplan-York estimate²⁵ of the fractal dimension $d_f \simeq 2.03$, see Ref.²⁶. Figure 1(a) shows a state-space portrait obtained by integration

of a random initial condition which converges, after a short transient, to the strange attractor.

For a continuous-time dynamical system with d -dimensional state-space, a Poincaré surface of section can be defined as a $(d-1)$ -dimensional hypersurface which intersects the flow transversally, supplemented by a condition for the direction of the crossing. For the Rössler flow a natural choice is a two-dimensional plane orthogonal to the (x, y) -plane. Introducing cylindrical coordinates (r, θ, z) , where $r^2 = x^2 + y^2$ and $\theta = \arctan(y/x)$, we illustrate two different Poincaré section choices $\mathcal{P}_1, \mathcal{P}_2$ defined by $\theta = -\pi/4$ and $\theta = \pi/4$, respectively, in Fig. 1(a). The corresponding points of intersection are shown in the two-dimensional plane (r, z) in Fig. 1(b,e) and can be used to define a *return map* R of successive intersections of the flow with the Poincaré section $R : (r_n, z_n) \mapsto (r_{n+1}, z_{n+1})$, where r_n denotes the value of r at the n 'th intersection, etc.. Since the points of intersection lie on an approximately one-dimensional curve one may attempt to reduce the dimension of the mapping by using a single coordinate, for example r , to construct a return map $R : r_n \mapsto r_{n+1}$. Such return maps R_1, R_2 corresponding to the sections $\mathcal{P}_1, \mathcal{P}_2$, respectively, are shown in Fig. 1(c,f).

The unimodal (i.e., having a single maximum) return map R_1 is approximately single valued, up to the “transverse structure” or “thickness” revealed in the inset of Fig. 1(c). The origin of this structure lies in the non-integer dimension of the attractor. In what follows we ignore this fine structure and consider such return maps to be one-dimensional and smooth. This approximation allows to apply the extensive set of tools developed for one-dimensional maps on the unit interval to return maps obtained from continuous-time flows by the Poincaré section method^{1,2}. By assigning the symbols 0 and 1 to points on the left and right, respectively, of the critical point r_c (the point that corresponds to the maximum of R_1), trajectories can be encoded as symbolic sequences or *itineraries*. We will forgo presenting the topological program in terms of the exhaustively studied Rössler system and come back to this point in the discussion of Kuramoto-Sivashinsky equation in Sec. III D, where we will also see that ignoring the transverse structure imposes limitations on the validity of this symbolic encoding for longer orbits.

By contrast to R_1 , the return map R_2 obtained using the section \mathcal{P}_2 , Fig. 1(f), cannot be considered approximately single-valued and is therefore not useful as a representation of the Rössler flow. The return map construction fails because the variable r does not vary monotonically for the points of intersection of the flow with \mathcal{P}_2 , cf. Fig. 1(f). This difficulty motivates the use of manifold learning for the parameterization of the Poincaré section.

B. Manifold learning

Manifold learning or nonlinear dimensionality reduction^{16,17} is a sub-field of unsupervised machine learning. The main problem it aims to address is projecting correlated data from a d -dimensional ambient space to a lower dimensional embedding space with dimension $d_r \ll d$, while preserving as

much of the structure in the data as possible. In other words, if the data are thought to lie on (or close to) a manifold embedded in the high-dimensional space, then manifold learning aims to re-embed this manifold to a space of as low a dimension as possible, while preserving either the geometrical or topological properties of that manifold. In contrast to linear dimensionality methods, such as principal component analysis, manifold learning methods utilize nonlinear transformations, which enables them to re-embed manifolds generated by nonlinear processes. A wide range of methods of nonlinear dimensionality reduction have been devised. Well known schemes which are of relevance to the study of nonlinear dynamical systems are Isomap²⁷, which aims to devise transformations which preserve geodesic distance on the manifold, diffusion maps^{19,28,29}, which are robust even in the presence of noise, and locally linear embedding (LLE)³⁰, which is a topology preserving method. Here we choose to use LLE because it is relatively efficient, a well documented implementation exists in the python package `scikit-learn`³¹ and topology (rather than distance) preservation is sufficient for our purposes. Similar results were also obtained for most cases studied here using Isomap.

LLE utilizes conformal mapping, which preserves local angles, in order to map data lying on (or close to) a manifold in a d -dimensional ambient space to the d_r -dimensional embedding space. The first step in the method is to select, for each data point, a neighborhood in which the manifold can be locally approximated as being linear. In practice this is achieved by detecting the K -closest neighbors of each data point, where K an integer threshold. This allows each data point to be reconstructed from its neighbors, up to a certain reconstruction error. The key observation on which LLE is based is that the coefficients (or “weights”) of the linear transformation used for the reconstruction are (under suitable constraints) invariant under rotations, translations and rescalings. Thus, these coefficients are expected to be identical for both the original and the low-dimensional embedding of the data. By minimizing the global reconstruction error, one obtains global intrinsic coordinates which parametrize the manifold in the low dimensional space. In practice, the problem of global error minimization is written in the form of a sparse eigenproblem of dimension $N_p \times N_p$, where N_p is the number of data points. The coordinates of the data points in the d_r -dimensional re-embedding space are then identified with the eigenvectors corresponding to the smallest d_r eigenvalues.

There are two free parameters in LLE: the number of neighbors kept K and a small normalization parameter δ . The latter is required in order to condition the eigenvalue problem when the number of neighbors K is larger than the number of ambient dimensions. Here, the parameter K is chosen by estimating the number of neighbors within an approximately linear neighborhood in the Poincaré section. It is noted that LLE can be formulated so that points within a ball of radius ϵ , rather than K -nearest neighbors, are kept as part of the linear neighborhood. While that formulation would be more well suited for the study of chaotic dynamics, for which data are not uniformly sampled, it has not been used here since it is not implemented in the present version of `scikit-learn`. The

normalization parameter δ was also varied and the construction of return maps repeated, in order to ensure that it leads to topologically equivalent results (by comparing kneading sequences, see Sec. II C). We note that there exist variants of LLE^{32,33}, which bypass the need for a normalization parameter at a slight increase in computational cost.

The computational cost of LLE (as implemented in `scikit-learn`) scales as $O[d \log(K) N_p \log(N_p)] + O[d N_p K^3] + O[d_r N_p^2]$, where the first term refers to the detection of K nearest neighbors, the second to the computation of local reconstruction weights and the third to the solution of the eigenvalue problem with dense methods³⁴. In `scikit-learn` the cost associated to the last term is significantly reduced through the use of sparse eigensolvers. The scaling with respect to the number of data points N_p makes it clear that it is much more efficient to first reduce the number of data points by introducing a Poincaré section and then perform LLE, rather than performing these operation in the reverse order.

C. Manifold learning of Poincaré sections

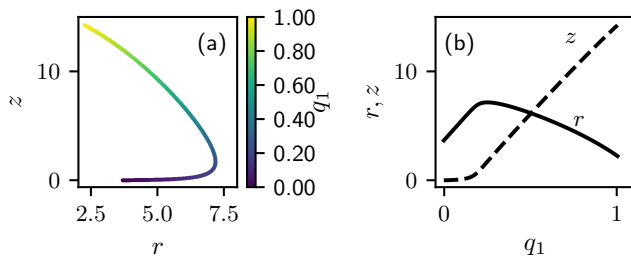


FIG. 2. (a) The points of intersection of the Rössler flow with the Poincaré section \mathcal{P}_2 parametrized by the intrinsic variable q_1 obtained by LLE. (b) Interpolating functions $r(q_1)$ and $z(q_1)$ allowing to inverse LLE in order to obtain points in the original state-space for any value of q_1 .

In the following we consider dynamical systems of the form

$$\dot{x} = F(x), \quad (4)$$

where $x \in \mathbb{R}^d$. We use as input (training) data \mathcal{D} the N_p points of intersection of the attractor of Eq. (4) with the $(d-1)$ -dimensional Poincaré surface of section. \mathcal{D} is a fractal set of non-integer dimension $d_f - 1$, where d_f is the fractal dimension of the attractor. Our aim is to use manifold learning in order to re-embed the data to a space of integer dimension d_r , providing intrinsic variables $q \in \mathbb{R}^{d_r}$. The embedding dimension d_r should be sufficiently high to allow the construction of a return map that captures the topology of the chaotic attractor. If some estimate of the attractor fractal dimension d_f is known, then the target dimension of the embedding space would be $d_r = \lfloor d_f - 1 \rfloor$, where $\lfloor \cdot \rfloor$ is the floor function. However, one does not need to rely on estimates of the attractor fractal dimension but could instead increase d_r iteratively until a single-valued return map is obtained, see Sec. III C. Here

we will restrict attention to cases for which we $d_r = 1$ or 2 is sufficient, but the same strategy is applicable for $d_r > 2$.

As a first application we consider the points of intersection of the Rössler flow with the Poincaré sections \mathcal{P}_1 and \mathcal{P}_2 . Application of LLE for both cases allows us to approximate the data of Fig. 1(b,e) as one-dimensional manifolds parametrized by a coordinate q , see Fig. 2. We can thus construct the one-dimensional return maps of Fig. 1(d,f), which are single valued even for the “problematic” section \mathcal{P}_2 (up to the thickness discussed in Sec. II A). The return maps of Fig. 1(c,d,f) describe the same dynamics and are thus conjugate to each other. We can show that this is indeed the case by examining the kneading sequence K_c , defined as the itinerary of the critical point, since two maps with the same kneading sequence are conjugate to each other¹. For all three maps of Fig. 1(c,d,f) we find the kneading sequences $K_c = 1001011111101 \dots$ to agree up to length at least 30.

We will often need to iterate the return maps constructed through the use of LLE for out-of-sample data. This requirement will be handled by either linear or nearest-neighbor interpolation between sample points. An example where this is useful is when locating period- p periodic orbits of the map by solving the condition $q_{1,n+p} = q_{1,n}$, through Newton–Raphson’s method.

There will also be occasions in which we need to extend the mapping $\mathcal{M} : x \mapsto q$, which relates in-sample data points to the LLE coordinates, to out-of-sample points. This would allow to use the return map to predict the evolution of state-space points that are not part of the training data. In `scikit-learn` this can be achieved without re-computing the full transform through a mapping procedure that computes reconstruction weights only for the out-of-sample points, as described in³⁵. A similar procedure can also be applied in order to construct an inverse LLE map $\mathcal{S} : q \mapsto x$, which is however not implemented in `scikit-learn`. Here we take a simpler approach based on the fact that all return maps in this work can be eventually parametrized by a single LLE coordinate q_1 (cf. Sec. III). Thus, it is sufficient to construct an inverse map as a set of d interpolating functions $\mathcal{S}_j : q_1 \mapsto x_j$, $j = 1, \dots, d$ using either nearest-neighbor or linear interpolation. Figure 2(a) and (b) illustrates the forward $\mathcal{M} : (r, z) \mapsto q_1$ and inverse $\mathcal{S}_1 : q_1 \mapsto r$, $\mathcal{S}_2 : q_1 \mapsto z$ maps, respectively, for the case of the Rössler example.

To illustrate the utility of the inverse map \mathcal{S} , suppose that we have obtained a root q_1^* of the condition $q_{1,n+1} = q_{1,n}$ for the return map of Fig. 1(d). This can then mapped to a point r^*, z^* on the Poincaré section by \mathcal{S}_j , $j = 1, 2$. This point is used as initial condition for Eq. (1) and integrated until the next intersection with the Poincaré section. The resulting solution is an approximation of a periodic orbit within plotting accuracy (that could be refined to desired accuracy by an iterative method²), as shown in Fig. 2(a). A more systematic procedure for the determination of periodic orbits up to a given period is provided in Appendix A and used in Sec. III.

Yet, one may argue that the Rössler example is somewhat artificial: Fig. 1(e) suggests that a usable return map could easily be constructed even for the case of section \mathcal{P}_2 by simply choosing z as the parameterizing variable. For this reason

we now turn to the discussion of application of manifold learning for Poincaré sections of a higher-dimensional system, for which simple parametrizations of the Poincaré section are not obvious, while the gains in dimensionality reduction will also be more significant.

III. APPLICATION TO KURAMOTO-SIVASHINSKY EQUATION

A. Kuramoto-Sivashinsky equation

The Kuramoto-Sivashinsky equation (KSe)^{36,37},

$$\partial_t u = (u^2)_x - u_{xx} - \nu u_{xxx}, \quad (5)$$

has received much attention as one of the simplest partial-differential equations (PDE) that exhibit spatiotemporally chaotic behavior. In Eq. (5), $u(x, t)$ is a one-dimensional scalar field, defined over a domain $x \in [-L/2, L/2]$ and ν is a damping parameter. Here we set $L = 2\pi$ and use ν as control parameter. An alternative choice common in the literature is to set $\nu = 1$ and use L as control parameter. One can convert between the two conventions through²² $\nu = (2\pi/L)^2$. Here we follow Ref.²¹ in imposing the Dirichlet boundary condition $u(-L/2, t) = u(L/2, t) = 0$, which restricts solutions to the subspace of antisymmetric functions, $u(x, t) = -u(-x, t)$. Fourier expanding

$$u(x, t) = \sum_{k=-\infty}^{+\infty} e^{ikx}, \quad (6)$$

taking into account the antisymmetry of $u(x, t)$, which implies $b_k = ia_k$ with a_k real, and substituting in Eq. (5) we obtain the infinite dimensional dynamical system

$$\dot{a}_k = (k^2 - \nu k^4) a_k - k \sum_{m=-\infty}^{+\infty} a_m a_{k-m}. \quad (7)$$

In numerical simulations Eq. (7) is truncated to a finite dimensional set of ordinary differential equations by setting $a_k = 0$ for $k > d$. Since $u(x, t)$ is real we have $a_k = -a_{-k}$ and choosing to work with zero-mean solutions, $a_0 = 0$, we obtain

$$\dot{a}_k = (k^2 - \nu k^4) a_k - k \left(\sum_{m=1}^{k-1} a_m a_{k-m} - \sum_{m=k+1}^d a_m a_{m-k} - \sum_{m=1}^{d-k} a_m a_{k+m} \right), \quad (8)$$

where $k = 1, \dots, d$. Note that with our conventions the real field $u(x, t)$ is sampled on $2(d+1)$ points, since $a_{d+1} = a_0 = 0$. For the range of parameters studied here $d = 16$ is sufficient for well resolved simulations²¹. In the following we will study attractors of this 16-dimensional truncation of KSe.

In the antisymmetric subspace, the continuous translational symmetry of KSe reduces to the discrete group of half-cell translations, $\tau u(x, t) = u(x + \pi, t)$ ^{38,39}. This implies that if $u(x, t)$ is a solution then $u(x + \pi, t)$ is also a solution. Therefore solutions of Eq. (5) either come in τ -related pairs or are

invariant (either pointwise or set-wise) under τ ⁴⁰. In terms of the Fourier modes half-cell translation symmetry takes the form

$$\tau a_{2m} = a_{2m}, \quad (9)$$

$$\tau a_{2m+1} = -a_{2m+1}, \quad (10)$$

where m is an integer. The study of the system can be greatly simplified if points in state space related by symmetry are identified, i.e., if we apply symmetry reduction^{2,41}. This can be achieved by either a suitable change of variables (e.g. to invariant polynomials⁴¹) or by introducing a fundamental domain⁴², a subspace of the full state space which contains exactly one copy of each symmetry related pair. The latter approach is sufficient for our purposes and can be most easily achieved after the introduction of a Poincaré section. However, care must be taken that the Poincaré section is a group-invariant set, so that no state-space points leave the section under a symmetry transformation. This can be achieved by imposing a group-invariant condition to define the Poincaré section⁴³. Here we use the Poincaré section

$$a_2 = 0, \quad (11)$$

subject to the orientation condition $\dot{a}_2 > 0$. Eq. (11) is invariant under the action Eq. (9) of τ . An example of using this surface of section in a KSe simulation with $\nu = 0.0299$ is shown in Fig. 3(a). We observe that the attractor consists of two distinct parts related by the action Eq. (9) of τ . This motivates the definition of the fundamental domain consisting of all points a with

$$a_3 \geq 0. \quad (12)$$

State space points that do not satisfy Eq. (12) are mapped to the fundamental domain by applying the half-cell translation operation $\tilde{a} = \tau a$, where τ is given by Eq. (9) and \tilde{a} denotes a point in the fundamental domain. This leads to the symmetry reduced Poincaré section of Fig. 3(b). In what follows we will simplify notation by referring to both points in the full space and the fundamental domain by the symbol a . We note that if we have chosen periodic boundary conditions then the symmetry group of KSe would be $O(2)$ and we would need to also implement continuous symmetry reduction^{23,44–46}.

In practice it is more efficient to use a pseudospectral evaluation⁴⁷ of the nonlinear term in Eq. (6), rather than the explicit sum in Eq. (8). Due to stiffness in KSe we use an implicit scheme based on a backward differentiation formula⁴⁸, as implemented in the library `scipy`⁴⁹. Variable time-step is used with absolute and relative tolerance set to 10^{-9} and 10^{-6} , respectively. It was checked that increasing these tolerances by an order of magnitude results in the same kneading sequences up to topological length at least 10 for the return maps presented here.

Return maps for KSe with Dirichlet boundary conditions have been studied in Ref.^{21,22}. In Ref.²¹ a one-dimensional return map is constructed for $\nu = 0.029910$, using the geodesic distance measured along an ordered set of points of periodic points on the Poincaré section. However, in this case a single

Fourier mode would also be sufficient for the parameterization of the return map. For a smaller value of the damping parameter, $\nu = 0.026634$, Ref.²² showed that there is considerably more complex structure in the attractor. The latter was decomposed in two parts, each parametrized by the geodesic distance along the one-dimensional unstable manifolds of two short periodic orbits, resulting in two disjoint one-dimensional return maps.

Here we choose to work with values of the damping parameter between these two extremes. The first case, with $\nu = 0.0299$ has a Poincaré section for which no obvious parameterization by a single Fourier mode could be found, yet can still be well approximated as one-dimensional using manifold learning. For the second case we choose $\nu = 0.02973$ which corresponds to one of the simplest cases for which a two-dimensional embedding is required.

B. One-dimensional embedding

For the first of the cases that we study we take $\nu = 0.0299$ and integrate KSe up to $t = 4000$, which results in $N_p = 9092$ intersection points with the Poincaré section. A projection of the Poincaré section in the full space and fundamental domain is shown in Fig. 3(a) and Fig. 3(b), respectively. The footprint of the attractor on the Poincaré section is extremely thin, suggesting that a one-dimensional embedding should be sufficient to represent the dynamics. However, Fig. 3(b) reveals no obvious variable for the construction of a return map. Manifold learning with LLE solves this problem in a natural way, allowing to construct a 1D embedding, visualized by the color-code used in Fig. 3(b). This results to a unimodal return map $q_n \mapsto q_{n+1}$ on the unit interval, shown in Fig. 3(c). The critical point x_c partitions the unit interval to two base intervals which we label with the symbols 0 and 1. The kneading sequence associated with the critical point is $K_c = 101111111\dots$ and will be used in Sec. III D to determine the spectrum of admissible periodic orbits.

We note that this map is only approximately unimodal, since the intersection of the attractor with the Poincaré section is only approximately one-dimensional, see the insets in Fig. 3(c) and (b), respectively. We see in particular that there is transverse structure in the return map of Fig. 3(c), where we can discern an “upper” or “primary” branch and a “lower” or “secondary” branch. The origin of these branches will be discussed in Sec. III E. Zooming in further would reveal additional structure (not shown). We could try to refine our description by keeping a second dimension in LLE, as we do for the lower damping parameter case in Sec. III C. However, this will not be necessary for the present example, since we will show in Sec. III D that the approximate one-dimensional map correctly encodes topological information on the spectrum of short periodic orbits of the system.

C. Two-dimensional embedding case: from a tree map to a trimodal map

For slightly smaller value of the damping parameter, $\nu = 0.02973$, KSe was integrated up to $t = 40000$, resulting in $N_p = 93640$ intersection points with the Poincaré section, shown in Fig. 4(a). A naive return map $q_{1,n} \mapsto q_{1,n+1}$, Fig. 4(c), using the first LLE embedding variable q_1 results in a return map which cannot be considered approximately single valued, i.e., we cannot ignore the secondary branch of the map. It should be noted that such return maps can still be studied if one augments them with grammar rules specifying whether the “upper” or “lower” branch of the map would be visited in the next intersection⁵⁰. However, this complicates the analysis of symbolic dynamics and we will instead develop a methodology that would allow to disentangle maps like the one in Fig. 4(c). The origin of the multivaluedness of this map can be traced back to Fig. 4(a), where we can see that due to the existence of a secondary branch in the Poincaré section, q_1 cannot uniquely parameterize all points on the section. A two dimensional embedding is thus computed through application of LLE on the Poincaré section data, as shown in Fig. 4(b), where q_1 and q_2 are the embedding variables. This would seem to imply that we need to construct a two-dimensional return map $(q_{1,n}, q_{2,n}) \mapsto (q_{1,n+1}, q_{2,n+1})$. However, an alternative route is taken here, which will allow us to construct a one-dimensional map on the unit interval with four-letter alphabet.

Our starting point is the observation that the embedding of Fig. 4(b) can be thought of as (approximately) having the topology of a tree with three edges, E_i , $i = 1, \dots, 3$, and an internal vertex V , see Fig. 5(a). Intuitively, we observe that edges E_1 and E_2 can be parametrized by q_1 while edge E_3 can be parametrized by q_2 . However, in order to realize such a parameterization of the computational data we need a way to uniquely assign data points to each edge. The availability of a two-dimensional LLE embedding space is particularly invaluable in this respect, since it makes the problem of assigning data to the different edges much more tractable than in the original 15-dimensional Poincaré section. To this end, we perform a linear fit of the data shown in the inset of Fig. 5(a) to obtain a curve \mathcal{C} which separates points on E_3 from points on E_1 and E_2 . Then a data point belongs to E_3 if it satisfies $q_2 < \xi(q_1)$, subject to the additional condition $q_1 < q_{1,c}$, or belongs to $E_1 \cup E_2$ otherwise. Here, $\xi(q_1)$ is the graph of \mathcal{C} and $q_{1,c}$ effectively defines the position of the vertex V , as discussed shortly.

With this construction we are now in position to identify which points on $E_1 \cup E_2$ are mapped on $E_1 \cup E_2$ and which on E_3 in the next intersection with the Poincaré section, and vice-versa. This allows to define three maps between edges of the tree:

1. $g : E_p \mapsto E_1 \cup E_2$, where $E_p \subset E_1 \cup E_2$. In terms of Fig. 5(a) the set E_p corresponds to all points in $E_1 \cup E_2$ except those encircled by the red ellipse and is parametrized by q_1 . The map $g : q_{1,n} \mapsto q_{1,n+1}$ is shown in Fig. 6(a).

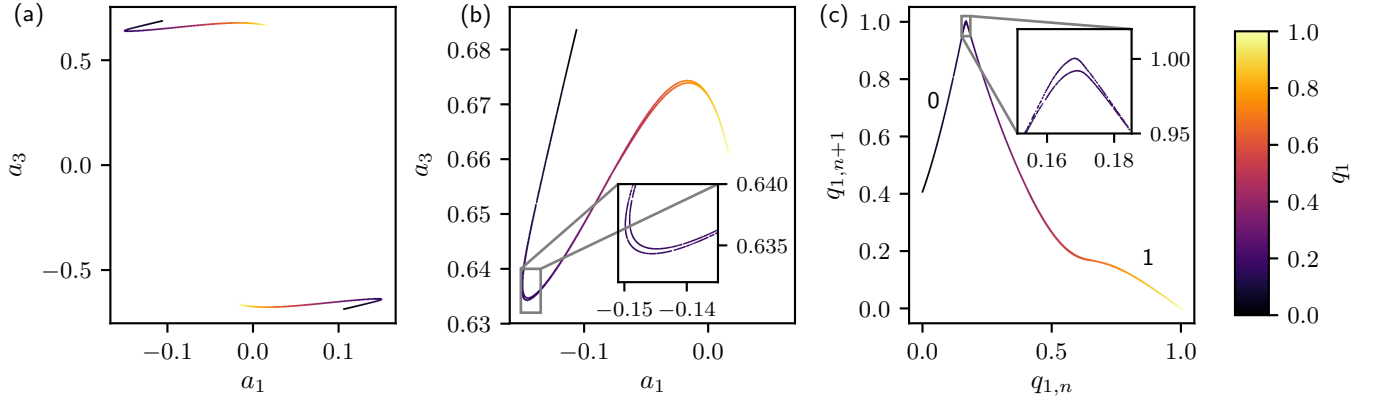


FIG. 3. KSe dynamics for $\nu = 0.0299$. (a) Full space Poincaré section, $a_1 - a_3$ modes projection, (b) Poincaré section reduced to the fundamental domain defined by $a_3 \geq 0$. (c) Return map using a 1D LLE embedding, with $K = 48$ nearest neighbors and regularization parameter $\varepsilon = 10^{-3}$.

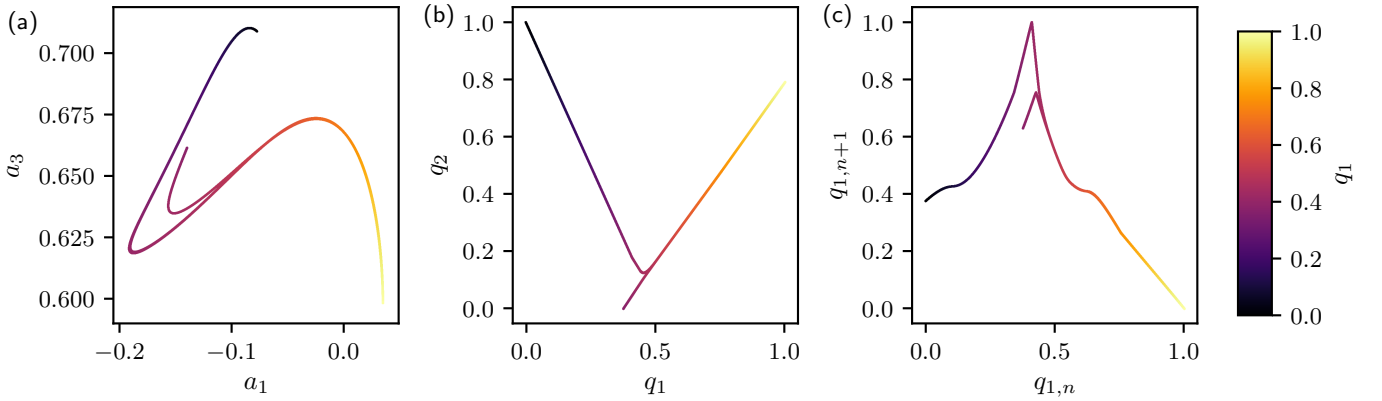


FIG. 4. (a) Projection of KSe Poincaré section on a_1, a_3 modes for $\nu = 0.02973$ (in the fundamental domain). (b) Two dimensional embedding of the Poincaré section on LLE coordinates (q_1, q_2) , using $K = 143$ nearest neighbors and regularization parameter $\varepsilon = 0.5 \times 10^{-3}$. (c) Naive return map using the coordinate q_1 is multi-valued.

2. $h : E_s \mapsto E_3$, where $E_s \subset E_1$ is encircled by the red ellipse in Fig. 4. The map $g : q_{1,n} \mapsto q_{2,n+1}$ is shown in Fig. 6(b).
3. $w : E_3 \mapsto E_r \subset E_2$. The graph of $w : q_{2,n} \mapsto q_{1,n+1}$ is shown Fig. 6(c). As will be discussed shortly, the restriction of the range of w to a subset of E_2 (rather than a subset of $E_1 \cup E_2$) can be achieved by a suitable choice of the position of the vertex V , through the parameter $q_{1,c}$, which defines the boundary between E_3 and E_2 . This choice allows to ensure continuity of the the combined map f , which will be constructed in the following.

We have thus constructed a description of the KSe attractor in terms of three coupled repellers approximated as maps on a tree. Such tree maps have appeared in the study of pruning of the Hénon map⁵¹. Since the kneading theory for such maps is quite involved⁵² a more direct approach is introduced here, which consists in using function composition in order to construct a single return map on the unit interval. In particular,

we define the map:

$$f(q_1) = \begin{cases} w(h(q_1)), & \text{if } q_1 < q_{1,c} \\ g(q_1), & \text{if } q_1 \geq q_{1,c}, \end{cases} \quad (13)$$

shown in Fig. 6(d). We have thus reduced the dynamics on the two-dimensional Poincaré section to a one-dimensional trimodal (i.e., having three maxima and minima) map on the interval. This map is approximately single-valued and continuous (up to fine structure similar to that discussed in Sec. III B). The continuity property can be imposed by a proper choice of the position of the vertex V . Since we deal here with a finite data set, we have some freedom to choose the position of this vertex, effectively changing the assignment of data points to different edges. We therefore choose a cutoff value $q_{1,c}$ which results in a continuous map, in the sense that any discontinuity in the map is of the order of the average distance between data points in our sample. If we had chosen a different a value $q'_{1,c} < q_{1,c}$ or $q'_{1,c} > q_{1,c}$, then we would have $w(h(q'_{1,c})) > g(q'_{1,c})$ or $w(h(q'_{1,c})) < g(q'_{1,c})$, respectively, and the map f would be discontinuous. While we could still

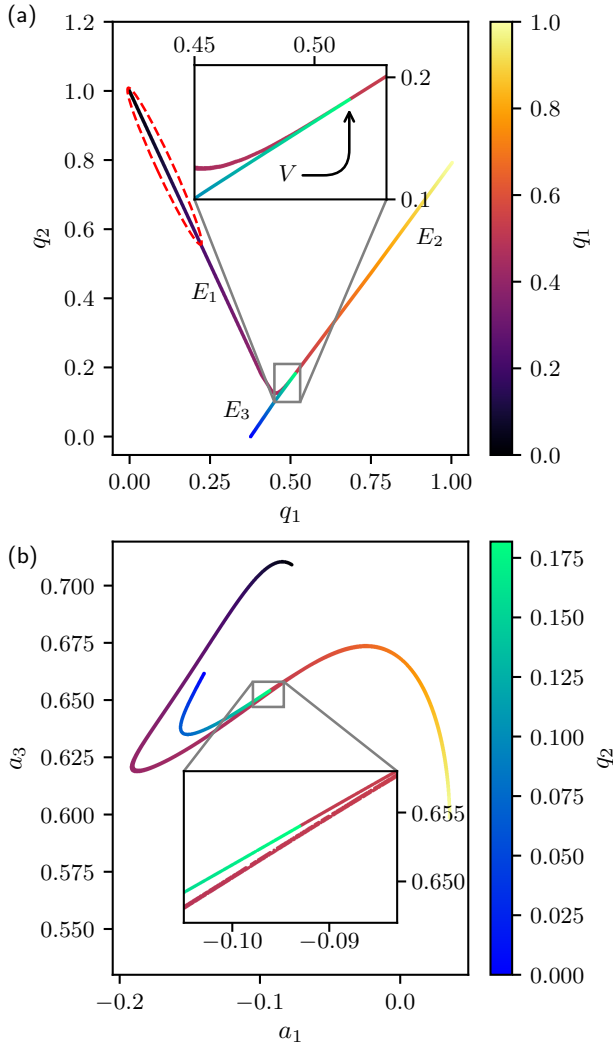


FIG. 5. (a) Two-dimensional LLE embedding of the Poincaré section of Fig. 4(b) interpreted as a tree with edges E_i , $i = 1, \dots, 3$, meeting at the vertex V (see inset). Points on edges E_1 and E_2 are parametrized (and color-coded) by the first LLE coordinate q_1 , while points on E_3 are parametrized (and color-coded) by the second coordinate q_2 . The red, dashed ellipse encloses the subset E_s of E_1 consisting of points mapped to E_3 in the next intersection with the Poincaré section. (b) Projection of KSe Poincaré section on a_1, a_3 modes, following the same color-coding as in panel (a).

obtain symbolic dynamics using a discontinuous map⁵³, our study is significantly simplified by ensuring continuity of f within the limits set by the finite sample size. Note that by this choice the tree topology is ensured for the two-dimensional LLE embedding but not necessarily for the original 15-dimensional Poincaré section, compare the insets in Fig. 5(a) and Fig. 5(b). As we will show, this choice to model the dynamics based on the LLE embedding rather than the original space correctly captures the spectrum of short (up to topological length $n = 10$) periodic orbits of the system, see Sec. III D. Note that the map f is not a first return map to the Poincaré section, but could be thought of as a first return map from the subset $E_1 \cup E_2$ to itself.

The three critical points $q_{i,c}$, $i = 1, \dots, 3$ partition the unit interval into four sub-intervals which can be assigned the symbols 0 to 4, as shown in Fig. 6(d). There are three corresponding kneading sequences, $K_1 = 3233303232\dots$, $K_2 = 3333333323\dots$ and $K_3 = 3032303230\dots$, which encode the topological organization of the flow and determine the spectrum of admissible periodic orbits, see Sec. III D. It was verified that the kneading sequences do not change up to topological length 10 when either the numerical integration tolerance parameters are reduced by an order of magnitude, integration time was increased by 50%, or LLE parameters were varied.

D. Periodic orbits

One of the advantages of representing continuous time dynamical systems with discrete time return maps, is that the latter allow the systematic determination of unstable periodic orbits which provide a skeleton of the dynamics and could be used in cycle expansions in order to compute average values of observables². For KSe in the antisymmetric domain there are two types of such solutions: periodic orbits with period T_p , satisfying $u(x, T_p + t) = u(x, t)$, and pre-periodic (or relative periodic) orbits $u(x, T_p + t) = \tau u(x, t)$, which are periodic of period $T_p' = 2T_p$ in the full space and of period T_p in the fundamental domain. We will refer to both types of orbits as *cycles* and distinguish them by their multiplicity in the full space: periodic orbits come in pairs related by half-cell translation τ (multiplicity $m = 2$), while pre-periodic orbits are τ -invariant sets (multiplicity $m = 1$).

For each fundamental domain cycle we can define its topological length n as the number of intersections of the orbit with the Poincaré section (restricted to $E_1 \cup E_2$ for the tree-topology case, $\nu = 0.02973$). Note that a cycle with multiplicity $m = 1$ and topological length n in the fundamental domain will have topological length $2n$ in the full space. If our discrete time return maps are indeed a valid representation of the continuous time flow then there must be a 1-1 correspondence between the return map cycles of period n and the flow cycles of topological length n . This allows us to both detect the cycles of the flow in a systematic manner and to test the limits of validity of the 1-D map approximation.

The procedure we follow in order to systematically detect cycles up to a given topological length is based on determining the admissible cycles through the well known kneading theory of one-dimensional maps⁵⁴, see^{1,2,50} for physicist-friendly expositions. In order to formulate guess periodic orbit solutions for an iterative solver we exploit the partitioning of the invariant interval to sub-intervals by the pre-images of the kneading sequence. Since this procedure has not, to the author's knowledge, been reported elsewhere it is briefly outlined in Appendix A.

For the KSe example with $\nu = 0.0299$ all cycles up to topological length $n = 8$ determined by kneading theory were found to correspond to cycles of the continuous time flow. Table I lists some of the shortest cycles as well as their leading Floquet multiplier (for pre-periodic orbits cycles this is computed in the fundamental domain) and their multiplicity.

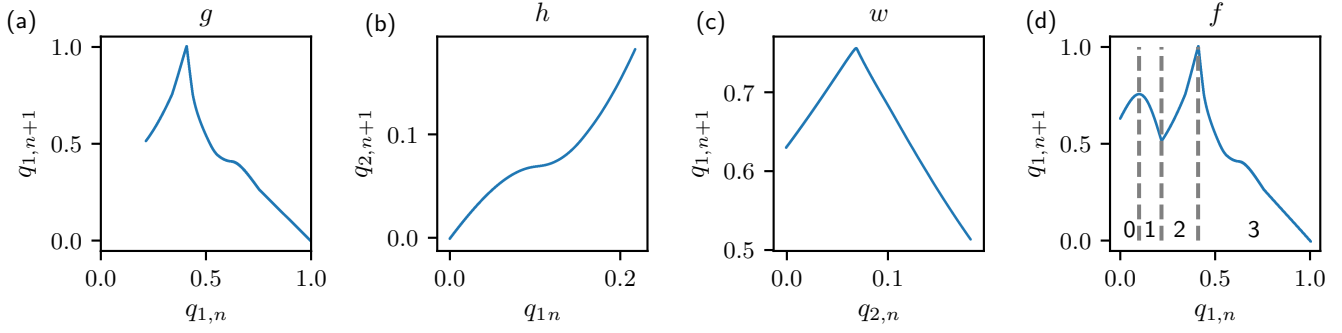


FIG. 6. Tree maps and combined map on the unit interval (a) map $g: E_p \mapsto E_1 \cup E_2$, (b) $h: E_r \mapsto E_3$, (c) $w: E_3 \mapsto E_2$, (d) $f: E_1 \cup E_2 \mapsto E_1 \cup E_2$. The dashed lines indicate the separation of the invariant interval $[0, 1]$ to sub-intervals corresponding to different symbols $s = 0, \dots, 3$.

TABLE I. All cycles up to topological length 6 for KSe, damping parameter $\nu = 0.0299$ (unimodal map) and $\nu = 0.02973$ (trimodal map). Listed are the cycle label p (overbars are dropped), fundamental domain period T_p , fundamental domain leading Floquet exponent Λ_1 and full-space cycle multiplicity m .

p	T_p	Λ_1	m
Unimodal, $\nu = 0.0299$			
1	0.449	-1.838	1
01	0.870	-2.085	2
0111	1.751	-4.206	2
010111	2.630	7.800	2
011111	2.640	-7.132	2
Trimodal, $\nu = 0.02973$			
3	0.447	-2.227	1
23	0.857	-3.230	2
1323	2.144	-10.792	1
1333	2.176	21.297	1
2333	1.737	-12.468	2
032323	2.980	-12.143	1
132323	2.995	21.210	1
133323	3.043	-79.969	1
133333	3.072	115.592	1
232333	2.599	41.663	2
233333	2.627	-54.925	2

At topological length $n = 10$, the boundary value solver did not converge for two of the cycles permitted by kneading theory, 0101111111 and 0111111111 . The reason for this is the transverse structure of the return map shown in the inset of Fig. 3(c), which implies additional pruning rules due to the secondary (lower) branch of the map. Indeed, the right-most point of each of these two cycles corresponds to topological coordinate θ exceeding that of the image of the critical point associated with the secondary branch, implying that both cycles are pruned (*cf.* Appendix A). In order to formulate such additional pruning rules in a consistent manner we would need to introduce a second LLE coordinate and eventually construct a multi-modal map, as we did for the case $\nu = 0.02973$. How-

ever, this was not attempted since we are interested here in the coarsest level of organization of the flow.

A finite grammar approximation of the symbolic dynamics for $\nu = 0.0299$ can be obtained by approximating the kneading sequence by $K_c = 10\bar{1}$. This leads to two forbidden sequences (pruning blocks), 00 and 0110 . The associated representation of the recurrent set symbolic dynamics as a finite automaton⁵⁰ is shown in Fig. 7. It correctly encodes all admissible periodic orbits up to length $n = 8$, but would need to be supplemented with additional rules at length $n = 10$. Using this graph the corresponding characteristic polynomial can be determined² to be

$$p(z) = 1 - 2z^2. \quad (14)$$

It allows us to compute the topological entropy $h = -\ln(z_0) \simeq 0.35$, where $z_0 = 1/\sqrt{2}$ solves $p(z_0) = 0$. The growth of the number of admissible intervals with topological length n found by admissibility criteria imposed by kneading theory (*cf.* Appendix A) is in good agreement with the estimate $\sim e^{hn}$; however, this should be considered an upper bound since additional pruning rules would need to be introduced for for $n > 8$.

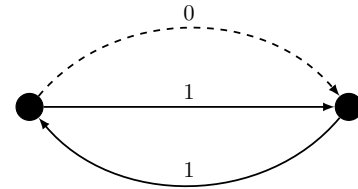


FIG. 7. Automaton representation of the finite grammar approximation of KSe recurrent set symbolic dynamics for $\nu = 0.0299$. Traversing a dashed line corresponds to symbol 0 while traversing a solid line corresponds to 1.

For the multi-modal map case, $\nu = 0.02973$, all admissible cycles of the discrete map up to length $n = 10$ led to converged searches for continuous time flow cycles. The shortest cycles, up to length $n = 6$ are listed in Tab. I, while two cycles are plotted in Fig. 8. In order to obtain reliable initial conditions

for the detection of some of the cycles of length $n = 10$ we had to increase the number of data points used in LLE (by increasing integration time) by 50%. The periodic orbit data (as well as the kneading sequences) suggest that symbols 0, 1, 2 and 3 are always followed by 3; however there exist multiple additional grammar rules of various lengths, suggesting that a useful finite grammar approximation might be out of reach in this case.

E. Organization of the flow in terms of unstable manifolds

One way to understand the topological organization of a chaotic flow is by tracking the stretching and folding of the unstable manifolds of compact solutions, such as periodic orbits². Unstable manifolds stretch due to local instability until they are folded by nonlinearity, without self-intersections. The process repeats itself creating the “transverse structure” in the Poincaré section of Fig. 3(b). An alternative, computationally more tractable way to understand this effect is by examining finite segments of the unstable manifolds of a few of the shortest cycles embedded in the attractor, as we now show.

All KSe cycles detected in this work have a single unstable direction associated with a real Floquet eigenvalue. For the unimodal map case, $\nu = 0.0299$, we plot in Fig. 9(a) segments of the global unstable manifolds $\mathcal{U}_{\bar{1}}$, $\mathcal{U}_{\bar{01}}$ of the two shortest cycles $\bar{1}$ and $\bar{01}$, respectively. These manifolds have been approximated by integrating forward in time 50 trajectories with initial conditions on the local unstable manifold of each cycle. We choose the integration time to be long enough to capture a significant segment of the global manifolds, yet short enough to avoid the inevitable nonlinear “folding” of the manifolds. As the inset in Fig. 9(a) shows each of these unstable manifolds spans a different “branch” of the transverse structure of the attractor. Longer cycles could be used to approximate the transverse structure with finer detail. The one-dimensional approximation amounts to disregarding the transverse structure. In this respect our treatment is similar to the parametrization of the the Poincaré section by the geodesic length along the unstable manifold of a short cycle proposed in Ref.²².

The trimodal map case, $\nu = 0.02973$, presents particular interest. Segments of the global unstable manifolds $\mathcal{U}_{\bar{3}}$, $\mathcal{U}_{\bar{23}}$ of the two shortest cycles $\bar{3}$ and $\bar{23}$, respectively, are plotted in Fig. 9(b). The unstable manifold $\mathcal{U}_{\bar{3}}$ spans much of the primary branch of the attractor (which we parameterized by q_1), while $\mathcal{U}_{\bar{23}}$ extends from the primary branch to the secondary branch (which we parameterized by q_2). The “misalignment” of these unstable manifolds leads to the need for a two-dimensional embedding. At the same time the fact that the unstable manifolds are one-dimensional explains why the tree approximation of the Poincaré section data was successful and led to the reduction of the dynamics to a one-dimensional map.

IV. CONCLUSIONS

In this work, it was shown through numerical examples that manifold learning can be used as a means to uncover the low-dimensional topological organization of high-dimensional chaotic dynamical systems by facilitating the construction of return maps. By contrast to previous work, nonlinear dimensionality reduction is applied directly on data on the Poincaré section, rather than on the continuous time attractor. This turns out to be computationally more efficient, as it significantly reduces the amount of data required, while preserving all information required for the construction of return maps. More importantly, it allows to decouple the problem of choosing a Poincaré section from the problem of parameterizing the return map, as discussed in Sec. II A. By introducing an intrinsic parameterization of the data, manifold learning allows one to choose any Poincaré section satisfying the minimal requirement of being transverse to the flow. If no single Poincaré section satisfying this requirement could be found, local sections could be used⁵⁵ and the resulting local maps combined as for the case of the tree maps of Sec. III C.

Application of the method on KSe allowed us to reduce the dynamics from the $d = 16$ -dimensional state-space in which well resolved solutions of the PDE live to one-dimensional maps. The latter enabled the systematic determination of the periodic orbits of the KSe flow, up to topological length $n = 10$. For the KSe example with lower value of the damping parameter, $\nu = 0.02973$, a two-dimensional embedding space for the Poincaré surface of section was required. Due to strong dissipation, the problem turned out to be quasi one-dimensional, with the data having the approximate topology of a tree. As a first step, a tree map was constructed which eventually was reduced to a one-dimensional trimodal map. The reason that this was possible was traced back to the fact that all unstable manifolds of periodic orbits, which organized the attractor, were one-dimensional. We may thus conjecture that for a wide class of systems possessing compact solutions with a low number of unstable directions a similar reduction procedure should be possible. The factor determining the dimensionality of the resulting return maps would be the maximal number of unstable directions, rather than the embedding dimension of the attractor.

ACKNOWLEDGMENTS

I would like to thank Alexander Jonsson, Caroline Bükk and Oscar Johansson for early contributions to this project and Predrag Cvitanović for inspiring discussions. This research has been supported by the Swedish Research Council, Grant No. 2016-05012.

DATA AVAILABILITY STATEMENT

The data that support the findings of this study are available from the author upon reasonable request. The code used

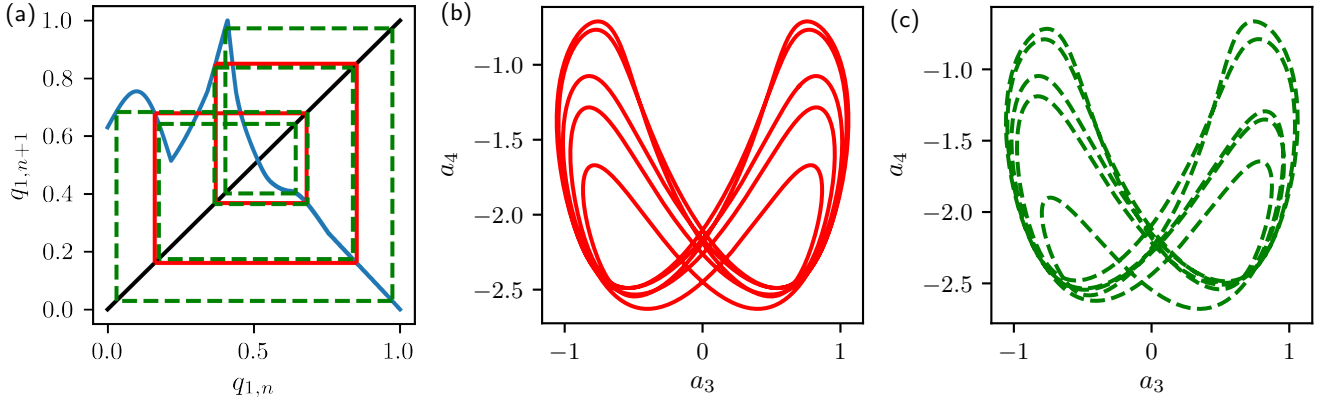


FIG. 8. KSe cycles for $\nu = 0.02973$. (a) Cycles $\overline{1323}$ (red, solid lines) and $\overline{03231323}$ (green, dashed lines) of the discrete time return map represented by 'cobwebs', (b,c) cycles $\overline{1323}$ and $\overline{03231323}$, respectively, of the continuous time flow, projected on a_3, a_4 modes.

in this work is available as a library in the online repository <https://github.com/vasimos/poinc-man>.

Appendix A: Methodology for periodic orbit searches

Here we outline the procedure developed for the systematic determination of periodic orbits of a continuous time flow, given a parameterization by an approximate one-dimensional map.

The first step is to determine the admissible cycles of topological length n . Consider a M -modal map f of the unit interval, with critical points $x_{c,i}$, $i = 1, \dots, M$, separating the invariant interval, here $I = [0, 1]$, to $N = M + 1$ base intervals I_k , $k = 0, \dots, M$ to each of which we associate a symbol $s = 0, \dots, M$. To simplify notation assume that the branches of f corresponding to even symbols are orientation preserving [$f'(x) > 0$], while those corresponding to odd symbols are orientation reversing [$f'(x) < 0$]. The algorithm can be easily adapted if this condition is not met. Take the following steps.

1. Determine the kneading sequences K_i of all critical points $x_{c,i}$ of the map, as well as the associated kneading values $\theta_i = \theta(K_i)$, where θ maps symbolic sequences to the so-called topological coordinate¹. The latter is defined for any symbolic sequence $\Sigma = s_0 s_1 \dots$ as

$$\theta(\Sigma) = \sum_{i=0}^{+\infty} \frac{t^i}{N^{i+1}},$$

where

$$t_i = \begin{cases} s_i, & \text{if } \varepsilon(s_0)\varepsilon(s_1)\dots\varepsilon(s_{i-1}) = 1, \\ (N-1) - s_i, & \text{if } \varepsilon(s_0)\varepsilon(s_1)\dots\varepsilon(s_{i-1}) = -1, \end{cases}$$

and the parity operator $\varepsilon(s_k) = 1$ ($\varepsilon(s_k) = -1$) if s_k is even (odd). The topological coordinate $\theta \in [0, 1]$ spatially orders symbolic sequences (both admissible and inadmissible ones).

2. Generate all prime cycle labels of length n using Duval's algorithm⁵⁶ to generate necklaces (periodic symbol sequences).
3. For each prime cycle label generate the symbolic sequences of all n cycle points by cyclic permutations of the cycle label.

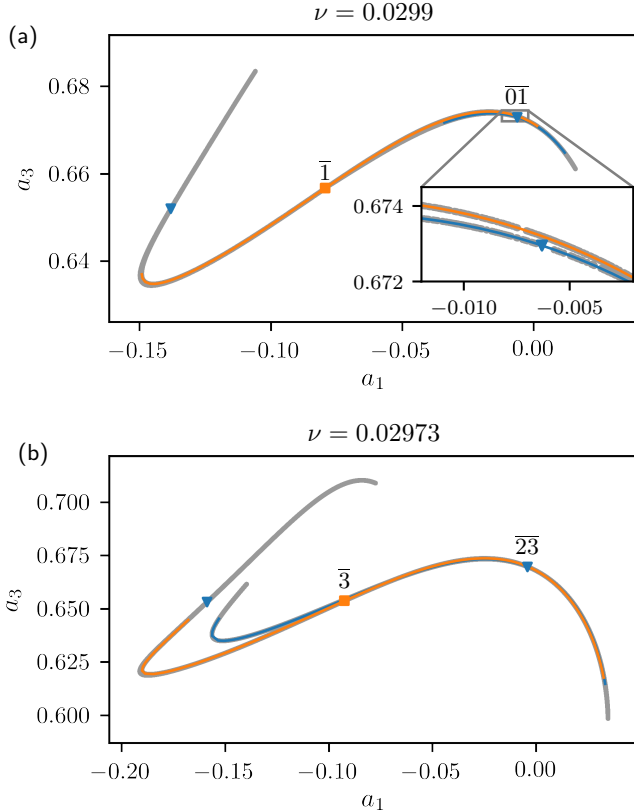


FIG. 9. (a) KSe Poincaré section projection for $\nu = 0.0299$, showing a long trajectory (grey), periodic points of cycles $\overline{1}$ (orange square) and $\overline{01}$ (blue triangles) and corresponding parts of their unstable manifolds, (orange/blue solid lines, respectively). (b) The same for $\nu = 0.02973$, showing periodic points of cycles $\overline{3}$ (orange square) and $\overline{23}$ (blue triangles) and corresponding parts of their unstable manifolds, (orange/blue solid lines, respectively). For cycles $\overline{01}$ and $\overline{23}$, only the part of the unstable manifold which connects to one of the periodic points has been visualized, for clarity.

4. We can use the fact that critical points are local maxima or minima of the map f in combination with spatial ordering of sequences by the topological coordinate θ to arrive at an admissibility condition for periodic orbits, see⁵⁰ for a readable review for multi-modal maps. For each critical point $x_{c,i}$ identify the set of all θ -points of a given cycle within the intervals I_{i-1}, I_{i+1} , i.e. to the left and right of the critical point. Denote by $s_0 s_1 \dots s_{n-1}$ the symbolic sequence of any cycle point within this set and by $s_1 \dots s_{n-1} s_0$ its forward image. Denote by $\theta^{\max}(s_1 \dots s_{n-1} s_0)$ [$\theta^{\min}(s_1 \dots s_{n-1} s_0)$] the maximum [minimum] value of the topological coordinate over the set of the forward images. Then a cycle is inadmissible if and only if there exists a critical point $x_{c,i}$ for which

$$\theta^{\max}(s_1 \dots s_{n-1} s_0) > K_i, \quad \text{for } i \text{ even}, \quad (\text{A1})$$

$$\theta^{\min}(s_1 \dots s_{n-1} s_0) < K_i, \quad \text{for } i \text{ odd}. \quad (\text{A2})$$

Having determined the set of admissible orbits we then need to generate initial guesses for the periodic points of the return map f . Our strategy is to determine, for each periodic point $s_0 s_1 \dots s_n$ of the map, sub-intervals $I_{s_0 s_1 \dots s_n}$ of the invariant interval I , which contain the periodic point. For single letter cycles ($n = 1$) these are the base intervals I_s , $s = 0, \dots, M$ in which the invariant interval is partitioned by the M critical points of the map f . For any admissible cycle of topological length $n > 1$ we:

1. Generate all possible symbolic sequences of points on the cycle (as above).
2. For cycle point with sequence $s_0 s_1 \dots s_n$, compute $I_{s_0 s_1 \dots s_n}$ recursively by application of the identity¹

$$I_{s_0 s_1 \dots s_n} = I_{s_0} \cap f_{s_0}^{-1}(I_{s_1 \dots s_n}),$$

where $f_{s_0}^{-1}$ is the inverse of the map f restricted to the base interval I_{s_0} (in which f is monotonic).

3. Take the midpoint of $I_{s_0 s_1 \dots s_n}$ as a guess for the cycle point $s_0 s_1 \dots s_n$.
4. Optionally, refine the guess by solving $f^n(q) = q$ through bisection or, for longer cycles, by setting up a multi-point shooting method².

Each admissible cycle of the return map can then be used to construct an initial ‘‘guess’’ solution, to be refined by an iterative method until it converges to the corresponding cycle of the continuous time flow (if the latter exists).

1. For each cycle point of the return map compute the corresponding full space point, through the the interpolating function $\mathcal{S} : q \mapsto x$, which maps LLE coordinates to ambient space coordinates $x \in R^d$ (Fourier modes a_i or the case of KSe). Note that in the case of 1D KSe embedding we construct d 1D interpolation functions $\mathcal{S}_i : q_1 \mapsto a_i$, $i = 1, \dots, d$. For the 2D embedding case of KSe with $v = 0.02973$, we only needed to perform

interpolation for points on E_1 and E_2 which are well parameterized by the first LLE coordinate q_1 ; this approach could be generalized to interpolate from q to a_i , if needed.

2. Use these approximate cycle points to set up a multiple-shooting or variational method to detect periodic orbits². In our implementation the collocation solver `solve_bvp` build into `scipy`⁴⁹ is used and solutions are detected in the full space, imposing the boundary condition $u(x, t + T_p) = u(x, t)$, with T_p undetermined. In order to prepare an initial time-periodic guess the Poincaré section cycle points are used as initial conditions which are integrated until the next intersection with the Poincaré section. Special care is taken to lift points from the fundamental domain to the full space in order to ensure continuity of the initial guess. The guess is refined to a prescribed error tolerance, here 10^{-6} .
3. Once a periodic orbit is found we check that it corresponds to the expected label by computing its intersections with the Poincaré section, mapping all points to the fundamental domain and computing the transform of these points to LLE variables q (this functionality is provided by the LLE implementation in `scikit-learn` without requiring recomputing the transform for all points in the dataset).

REFERENCES

- ¹R. Gilmore and M. Lefranc, *The Topology of Chaos* (Wiley, New York, 2003).
- ²P. Cvitanović, R. Artuso, R. Mainieri, G. Tanner, and G. Vattay, *Chaos: Classical and Quantum* (Niels Bohr Inst., Copenhagen, 2020).
- ³G. Kawahara and S. Kida, *J. Fluid Mech.* **449**, 291 (2001).
- ⁴D. Viswanath, *J. Fluid Mech.* **580**, 339 (2007).
- ⁵J. F. Gibson, J. Halcrow, and P. Cvitanović, *J. Fluid Mech.* **611**, 107 (2008).
- ⁶N. B. Budanur, K. Y. Short, M. Farazmand, A. P. Willis, and P. Cvitanović, *J. Fluid Mech.* **833**, 274 (2017).
- ⁷B. Suri, L. Kageorge, R. O. Grigoriev, and M. F. Schatz, *Phys. Rev. Lett.* **125**, 064501 (2020).
- ⁸M. D. Graham and D. Floryan, *Annu. Rev. Fluid Mech.* **53**, 227 (2021).
- ⁹K. A. Takeuchi, H. L. Yang, F. Ginelli, G. Radons, and H. Chaté, *Phys. Rev. E* **84**, 046214 (2011).
- ¹⁰X. Ding, H. Chaté, P. Cvitanović, E. Siminos, and K. A. Takeuchi, *Phys. Rev. Lett.* **117**, 024101 (2016).
- ¹¹C. Foias, G. R. Sell, and R. Témam, *J. Diff. Equ.* **73**, 309 (1988).
- ¹²C. Foias, B. Nicolaenko, G. R. Sell, and R. Témam, *J. Math. Pure Appl.* **67**, 197 (1988).
- ¹³P. Constantin, C. Foias, B. Nicolaenko, and R. Témam, *Integral Manifolds and Inertial Manifolds for Dissipative Partial Differential Equations* (Springer, New York, 1989).
- ¹⁴P. Holmes, J. L. Lumley, and G. Berkooz, *Turbulence, Coherent Structures, Dynamical Systems and Symmetry* (Cambridge Univ. Press, Cambridge, 1996).
- ¹⁵J. F. Gibson, *Dynamical-systems Models of Wall-bounded, Shear-flow Turbulence*, Ph.D. thesis, Cornell Univ. (2002).
- ¹⁶J. A. Lee and M. Verleysen, *Nonlinear Dimensionality Reduction*, Information Science and Statistics (Springer, New York, 2007).
- ¹⁷A. J. Izenman, *Wiley Interdiscip. Rev. Comput. Stat.* **4**, 439 (2012).
- ¹⁸E. Bollt, *Int. J. Bifur. Chaos* **17**, 1199 (2007).
- ¹⁹B. Nadler, S. Lafon, R. R. Coifman, and I. G. Kevrekidis, *Appl. Comput. Harmon. Anal.* **21**, 113 (2006).

- ²⁰C. J. Dsilva, R. Talmon, R. R. Coifman, and I. G. Kevrekidis, *Appl. Comput. Harmon. Anal.* **44**, 759 (2018).
- ²¹F. Christiansen, P. Cvitanović, and V. Putkaradze, *Nonlinearity* **10**, 55 (1997).
- ²²Y. Lan and P. Cvitanović, *Phys. Rev. E* **78**, 026208 (2008).
- ²³E. Siminos and P. Cvitanović, *Physica D* **240**, 187 (2011).
- ²⁴O. E. Rössler, *Phys. Lett. A* **57**, 397 (1976).
- ²⁵J. L. Kaplan and J. A. Yorke, in *Functional Differential Equations and Approximation of Fixed Points*, Lect. Notes Math., Vol. 730, edited by H.-O. Peitgen and H.-O. Walther (Springer, Berlin, 1979) pp. 204–227.
- ²⁶N. V. Kuznetsov, T. N. Mokaev, and P. A. Vasilyev, *Commun. Nonlinear Sci. Numer. Simul.* **19**, 1027 (2014).
- ²⁷J. B. Tenenbaum, V. d. Silva, and J. C. Langford, *Science* **290**, 2319 (2000).
- ²⁸R. R. Coifman, S. Lafon, A. B. Lee, M. Maggioni, B. Nadler, F. Warner, and S. W. Zucker, *PNAS* **102**, 7426 (2005).
- ²⁹R. R. Coifman and S. Lafon, *Applied and Computational Harmonic Analysis Special Issue: Diffusion Maps and Wavelets*, **21**, 5 (2006).
- ³⁰S. T. Roweis and L. K. Saul, *Science* **290**, 2323 (2000).
- ³¹F. Pedregosa, G. Varoquaux, A. Gramfort, V. Michel, B. Thirion, O. Grisel, M. Blondel, P. Prettenhofer, R. Weiss, V. Dubourg, J. Vanderplas, A. Passos, D. Cournapeau, M. Brucher, M. Perrot, and E. Duchesnay, *Journal of Machine Learning Research* **12**, 2825 (2011).
- ³²D. L. Donoho and C. Grimes, *PNAS* **100**, 5591 (2003).
- ³³Z. Zhang and J. Wang, *Advances in neural information processing systems* **19**, 1593 (2007).
- ³⁴<https://scikit-learn.org/stable/modules/manifold.html>.
- ³⁵L. K. Saul and S. T. Roweis, *J. Mach. Learn. Res.* **4**, 119 (2003).
- ³⁶Y. Kuramoto and T. Tsuzuki, *Progr. Theor. Phys.* **55**, 356 (1976).
- ³⁷G. I. Sivashinsky, *Acta Astronaut.* **4**, 1177 (1977).
- ³⁸I. G. Kevrekidis, B. Nicolaenko, and J. C. Scovel, *SIAM J. Appl. Math.* **50**, 760 (1990).
- ³⁹P. Cvitanović, R. L. Davidchack, and E. Siminos, *SIAM J. Appl. Dyn. Syst.* **9**, 1 (2010).
- ⁴⁰M. Golubitsky and I. Stewart, *The Symmetry Perspective* (Birkhäuser, Boston, 2002).
- ⁴¹R. Gilmore and C. Letellier, *The Symmetry of Chaos* (Oxford Univ. Press, Oxford, 2007).
- ⁴²P. Cvitanović and B. Eckhardt, *Nonlinearity* **6**, 277 (1993).
- ⁴³E. Siminos, *Recurrent Spatio-temporal Structures in Presence of Continuous Symmetries*, *Ph.D. thesis*, School of Physics, Georgia Inst. of Technology, Atlanta (2009).
- ⁴⁴C. W. Rowley and J. E. Marsden, *Physica D* **142**, 1 (2000).
- ⁴⁵W.-J. Beyn and V. Thümmler, *SIAM J. Appl. Dyn. Syst.* **3**, 85 (2004).
- ⁴⁶N. B. Budanur, P. Cvitanović, R. L. Davidchack, and E. Siminos, *Phys. Rev. Lett.* **114**, 084102 (2015).
- ⁴⁷J. P. Boyd, *Chebyshev and Fourier Spectral Methods*, 2nd ed. (Dover, New York, 2000).
- ⁴⁸L. F. Shampine and M. W. Reichelt, *SIAM J. Sci. Comput.* **18**, 1 (1997).
- ⁴⁹P. Virtanen, R. Gommers, T. E. Oliphant, M. Haberland, T. Reddy, D. Cournapeau, E. Burovski, P. Peterson, W. Weckesser, J. Bright, S. J. van der Walt, M. Brett, J. Wilson, K. J. Millman, N. Mayorov, A. R. J. Nelson, E. Jones, R. Kern, E. Larson, C. J. Carey, Í. Polat, Y. Feng, E. W. Moore, J. VanderPlas, D. Laxalde, J. Perktold, R. Cimrman, I. Henriksen, E. A. Quintero, C. R. Harris, A. M. Archibald, A. H. Ribeiro, F. Pedregosa, P. van Mulbregt, and SciPy 1.0 Contributors, *Nature Methods* **17**, 261 (2020).
- ⁵⁰K. T. Hansen, *Symbolic Dynamics in Chaotic systems*, *Ph.D. thesis*, Univ. of Oslo, Oslo, Norway (1993).
- ⁵¹A. de Carvalho and T. Hall, *Nonlinearity* **15**, R19 (2002).
- ⁵²J. F. Alves and J. S. Ramos, *Ergod. Theory Dyn. Syst.* **24**, 957 (2004).
- ⁵³L. Sella and P. Collins, *J. Comput. Appl. Math.* **234**, 418 (2010).
- ⁵⁴J. Milnor and W. Thurston, in *Dynamical Systems (Maryland 1986-87)*, edited by A. Dold and B. Eckmann (Springer, New York, 1988) pp. 465–563.
- ⁵⁵P. Cvitanović, D. Borrero-Echeverry, K. Carroll, B. Robbins, and E. Siminos, *Chaos* **22**, 047506 (2012).
- ⁵⁶J.-P. Duval, *Theoret. Comput. Sci.* **60**, 255 (1988).